Highly active Ptx(SnO2)100-x/C catalysts towards the hydrogen oxidation reaction and tolerant to the presence of carbon monoxide

Koffi Franck Bouho, Weliton Silva Fonseca, Sirine Ben Latifa, Thibault Rafaïdeen, Frédéric Pailloux, Julie Rousseau, Christine Canaff, Sophie Morisset, Têko Napporn, Christophe Coutanceau

To cite this version:

Koffi Franck Bouho, Weliton Silva Fonseca, Sirine Ben Latifa, Thibault Rafaïdeen, Frédéric Pailloux, et al.. Highly active Ptx(SnO2)100-x/C catalysts towards the hydrogen oxidation reaction and tolerant to the presence of carbon monoxide. Materials & Design, 2025, 260, pp.115194. ⟨10.1016/j.matdes.2025.115194⟩. ⟨hal-05383828⟩

HAL Id: hal-05383828
https://hal.science/hal-05383828v1

Submitted on 26 Nov 2025

Materials & Design 260 (2025) 115194

Contents lists available at ScienceDirect

Materials & Design

journal homepage: www.elsevier.com/locate/matdes

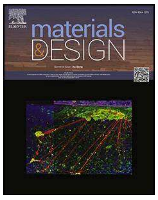

Highly active $Pt_x(SnO_2)_{100-x}/C$ catalysts towards the hydrogen oxidation reaction and tolerant to the presence of carbon monoxide

Franck Koffi Bouho [a], Weliton Silva Fonseca [a], Sirine Ben Latifa [a], Thibault Rafaïdeen [a], Frédéric Pailloux [b], Julie Rousseau [a], Christine Canaff [a], Sophie Morisset [a], Têko W. Napporn [a,c], Christophe Coutanceau [a,c,*]

[a] Université de Poitiers, IC2MP, UMR CNRS 7285, 86073 Cedex 9 Poitiers, France
[b] Institut Pprime, Université de Poitiers-CNRS-ENSMA, UPR 3346, France
[c] French Research Network on Hydrogen (FRH2), Research Federation No. 2044 CNRS, France

ARTICLE INFO

Keywords:
CO
EMSI
HOR
PEMFC
Platinum
Tin oxide
Tolerance

ABSTRACT

$Pt_x(SnO_2)_{100-x}/C$ materials consist of 1.5 to 2.5 nm nanoparticles deposited on a carbon support and decorated by SnO_2. Pt and Sn are slightly alloyed (5 % to 8 %) in nanoparticles. From XPS study the Sn 3d peaks present a shift towards lower binding energy values, indicating clearly an electron transfer from Pt(PtSn) towards SnO_2 (electronic metal support interaction – EMSI). The incorporation of SnO_2 into Pt enhances the catalytic activity towards the HOR at 0.02 V *vs.* RHE. The mass activity doubles, increasing from 147 mA mg_{Pt}^{-1} for Pt/C to 286 mA mg_{Pt}^{-1} for $Pt_{50}(SnO_2)_{50}/C$, while the specific activity increases fourfold, from 0.33 mA cm_{Pt}^{-2} to 1.33 mA cm_{Pt}^{-2}. These enhancements are attributed to EMSI. $Pt_x(SnO_2)_{100-x}/C$ catalysts exhibit lower onset potentials for CO_{ads} removal compared to Pt/C, both in the absence and presence of hydrogen. The high rate of CO removal is attributed to the bifunctional mechanism, while the shift of the CO_{ads} oxidation onset potential towards lower values from a ligand effect. At 60 °C, all catalysts show activity for the HOR from 0.05 V *vs.* RHE in the presence of CO. Among them, $Pt_{50}(SnO_2)_{50}/C$ demonstrates the highest HOR activity and the greatest CO tolerance.

1. Introduction

Three decades after the Rio conference, the world experiences the effects of climate change disruption caused by the accumulation of greenhouse gases in the atmosphere. To limit the global warning below 2 °C at the end of the century, the European Union has signed the Green Deal, aiming for carbon neutrality by 2050 [1–3]. Therefore, a transition toward more environmentally friendly energy sources is necessary. In this context, proton exchange membrane fuel cell (PEMFC) technology fed with green hydrogen (produced from renewable energy sources) can be a good alternative as energy supplier. Indeed, PEMFC can produce electrical energy without carbon dioxide (CO_2) emissions [4]. It is a mature technology that offers numerous advantages in terms of efficiency and power density, facilitating its use in automotive, stationary and aerospace applications. The main reactions taking place within a PEMFC are the hydrogen oxidation reaction (HOR) at the anode and the oxygen reduction reaction (ORR) at the cathode [5]. The overall reaction produces water, electricity and heat according to equation (1):

$$H_2 + O_2 \rightarrow H_2O + \text{Electricity} + \text{Heat} \quad (1)$$

The democratisation of the PEMFC technology requires the reduction of electrode manufacturing costs, particularly because they contain platinum (Pt). Indeed, Pt is the most active metal for both the HOR and ORR in acidic environment. Gasteiger et al. [6] showed that reducing the Pt loading in anode down to 0.05 mg cm^{-2} did not result in any voltage loss when using pure hydrogen (H_2). However, the presence of impurities in hydrogen, such as carbon monoxide (CO), CO_2, hydrogen sulphide (H_2S), etc., even as trace amounts, leads to decrease dramatically the performance of PEMFCs [7–10]. Currently, H_2 is mainly produced from steam reforming of natural gas, and contains *ca.* 1 % CO after the water gas shift reactions. Papageorgopoulos and De Bruijn [11] showed that 1 % CO in H_2 reformate poisons 98 % of the active surface sites of a Pt catalyst used at the anode of the fuel cell. As contamination by CO is a major problem in PEMFC technology, new anodic CO-tolerant Pt-based catalysts modified by metals with oxyphilic properties have emerged [12–16], amongst them platinum-tin (PtSn) materials because Sn is less expensive than ruthenium (Ru), and more efficient in term of CO-

---

[*] Corresponding author at: Université de Poitiers, IC2MP, UMR CNRS 7285, 86073 Cedex 9 Poitiers, France.
E-mail address: christophe.coutanceau@univ-poitiers.fr (C. Coutanceau).

https://doi.org/10.1016/j.matdes.2025.115194
Received 26 August 2025; Received in revised form 24 October 2025; Accepted 20 November 2025

tolerance [17,18].

If metallic Sn possesses a good electronic conductivity, it is not very stable in acidic media; it suffers from corrosion and oxidizes easily in air. Tin oxide (SnO_2) is a n-type semiconductor [19], which offers interesting properties for PEMFC applications. Zhang et al. [20] synthesized SnO_2 with a high surface area (205 m^2 g^{-1}) and used it as a support for Pt nanoparticles (NPs). They showed that SnO_2 promoted good dispersion of the Pt NPs, and they obtained equivalent activity and better stability for the HOR than with classical Pt/C catalysts. Dou et al. [21] drawn the same conclusions using tin oxide nanocluster (SnO_2) with parallel nanorods as anode catalyst support for PEMFCs. The possibility of a strong metal support interaction (SMSI) or electronic metal support interaction (EMSI) was recently proposed to explain the improved electrochemical properties of Pt-SnO_2 composites [22]. SMSI/EMSI has been evidenced through the improvement of durability and stability of Pt NPs decorating WO_3 nanoplatelets, as well as through the enhancement of the HOR activity. These improvements have been indeed explained in terms of synergetic effects and H spill over [23]. In both these cases, the SMSI/EMSI effect was explained in terms of shift of the Pt d-band centre due to electron transfer from the oxide support towards Pt nanoparticles. The second interest of using SnO_2 as catalyst support is related to its oxidizing properties, which could promote the electro-oxidation of CO to CO_2. [24] Metal oxides have been shown to improve, for example, alcohol oxidation by decreasing the development of adsorbed carbon monoxide (CO_{ads}) on the catalyst surface. [25,26].

Despite extensive studies, the mechanism underlying the high CO tolerance of $Pt_x(SnO_2)_{100\text{-}x}/C$ catalysts remains debated. Some authors attribute it to the electronic (ligand) effect, where SnO_2 incorporation modifies the Pt electronic structure (ESMI), weakening the Pt–CO_{ads} bond. Others emphasize the bifunctional mechanism, in which tin oxides dissociate water (H_2O) and generate adsorbed hydroxyl species (OH_{ads}) at lower potentials than Pt, thereby promoting CO_{ads} oxidation [24,27–29].

This study aims to clarify which mechanism predominates for both hydrogen oxidation and CO_{ads} oxidation on $Pt_x(SnO_2)_{100\text{-}x}/C$ catalysts. For this purpose, catalytic materials of different atomic compositions, $Pt_x(SnO_2)_{100\text{-}x}/C$, are synthesized by a polyol method and comprehensively characterised by different physicochemical techniques, including thermogravimetry analysis (TGA), inductive coupled plasma – optical emission spectroscopy (ICP-OES), high resolution transmission electron microscopy (HR-TEM), energy dispersive x-ray spectroscopy (EDS), energy filtered selected area electron diffraction (EF SAED), x-ray diffraction (XRD) and x-ray photoemission spectroscopy (XPS). Then, the electrochemical behaviours of the catalysts towards the HOR in the absence and in the presence of CO are assessed by cyclic voltammetry (CV), linear scan voltammetry (LSV) and chronoamperometry (CA), and results compared with the objective to further propose a structure/reactivity relationship and reaction mechanisms.

2. Experimental

2.1. Catalysts preparation

The synthesis of catalytic materials is split into two distinct steps. The first step consists in synthesising the SnO_2 colloid. It involves dissolving a given mass of tin chloride salt ($SnCl_2 \cdot 2H_2O$, Sigma Aldrich, purity > 98.9 %) in ethylene glycol (puriss. p.a., purity > 99.5 % from Fluka) for 2 h under magnetic stirring and adjusting the pH of the medium to 7–8 using a 1 M sodium hydroxide (NaOH, semiconductor grade, 99.99 % purity, Sigma-Aldrich) in ethylene glycol (EG) solution. Then the mixture is heated at reflux (*ca.* 190 °C) for 2 h with oxygen (O_2) bubbling (U Quality from Air Liquide). The light-yellow coloration confirms the formation of tin oxide NPs.

The second step involves the dissolution of hexachloroplatinic acid ($H_2PtCl_6 \cdot 6H_2O$, 99.9 % purity from Alfa Aesar) in EG for half an hour under magnetic stirring, the adjustment of the pH to 11 with a 1 M NaOH in EG solution, and the addition of a given volume of the previous SnO_2 colloidal solution to achieve nominal molar ratios of Pt_{100}, $Pt_{90}(SnO_2)_{10}$, $Pt_{65}(SnO_2)_{35}$ and $Pt_{50}(SnO_2)_{50}$. The mixture is then heated at 160 °C for 2 h. Once the temperature has decreased to room temperature, a mass of carbon Vulcan XC 72 (Cabot Corp.) pre-treated at 400 °C under nitrogen (N_2, U quality from Air Liquid) flow for 4 h is added to reach a metal loading of 40 wt%. Finally, the mixture is washed with ultra-pure (UP) water (MilliQ, Millipore, 18.2 MΩ cm) and acetone (> 99 %, WWR Chemicals), then dried at 60 °C for 2 h.

2.2. Physicochemical characterisation

TGA are performed to determine the material metal loadings with a TA Instrument model SDT Q 600. Measurements were carried out under air flow at 100 mL min^{-1} between 25 °C and 800 °C with a temperature ramp of 10 °C min^{-1}.

XRD analyses are carried out using a PANalytical diffractometer in Bragg-Bentano configuration, equipped with a Cu anode powered at 45 kV and 40 mA. Measurements are recorded between 20° and 80° with steps of 0.083° and an acquisition time of 2 s.

ICP-OES analyses are carried out using a 5110 Agilent VDV apparatus to determine the bulk atomic ratio of Pt and Sn.

TEM was carried out using a JEOL (200 keV) model JEM 2100 with a LaB_6 gun (maximum resolution of 0.19 nm). HRTEM, EDS mapping and energy filtered selected area electron diffraction (EF-SAED) analysis were performed using a JEM 220FS TEM/STEM equipped with a shottky-FEG operated at 200 kV and fitted with an in-column omega-filter. EF-SAED diffractograms were recorded on a GATAN-OneView CMOS camera; the width of the slit for energy-filtering was set to 10 eV around the zero-loss peak to get rid of the strong inelastic scattering coming from the thick carbon support. EDS spectra and maps were acquired with a 60 mm^2 Bruker X-FLASH SDD; a single–tilt Be-holder was used to minimize the background contribution and spurious signals coming from the TEM. For elemental mapping, the electron probe size was set to 1.5 nm. High angle annular dark-field scanning transmission electron micrographs (HAADF-STEM) were obtained simultaneously.

XPS analysis were carried out with a Kratos Axis Ultra DLD spectrometer using a monochromatic Al K_α source (1486.6 eV) operating at 180 W (12 mA, 15 kV). Pressure in analytic chamber was 9×10^{-8} Pascal. High-resolution spectra were recorded using an analysis area of 300 μm × 700 μm and 40 eV pass energy. This pass energy corresponds to Ag 3d5/2 FWHM of 0.55 eV. Data were acquired with 0.1 eV steps. The measurements were performed without using the charge neutralizer because all samples were conductive. The binding energy scale and spectrometer work function were calibrated previously with pure gold foil. The following binding energies regions were recorded: C 1 s, O 1 s, Sn 3d and Pt 4f. Atomic ratios were calculated using sensitivity factors provided by the manufacturer. Peak fitting was achieved using Casa XPS software (version 2.3.26) applying Gaussian-Lorentzian profiles (Lorentzian 30 % and 60 %). Prior to quantification, the background was subtracted with a Shirley function.

2.3. Electrochemical characterisation

All electrochemical measurements are performed at the controlled temperature of 25 °C in a 0.1 M $HClO_4$ (Suprapur, Merck) in UP water supporting electrolyte using an interfaced Autolab PGSTAT302N potentiostat (Metrohm). The standard three-electrode electrochemical cell is fitted with a reversible hydrogen electrode (RHE, HydroFlex from Gaskatel) as the reference electrode and a glassy carbon plate (2 cm^2 geometric surface area) as the counter electrode. The working electrode consists of a glassy carbon rotating disc of 0.196 cm^2 geometric surface area (RDE GC50.S, Metrohm) on which the catalytic layer is deposited. The catalytic ink is composed of 5 mg of a catalytic powder dissolved in 750 μL of UP water, 250 μL of 2-propanol (anhydrous 99.5 %, Sigma-Aldrich) and 100 μL of Nafion® solution (5 %wt. in aliphatic alcohol from Aldrich). The mixture is homogenised in an ultrasonic bath (Fisherbrand 15,051 ultrasonic bath, 2.75 L, 37 kHz, 320 W) for 30 min, and 5 μL of the catalytic ink are deposited from a syringe onto a freshly polished glassy carbon substrate. The solvent is evaporated in a N_2 flow at the electrode rotation rate of 400 rpm (revolution per minute).

Cyclic voltammograms (CVs), linear scan voltammograms (LSVs) and CO (N47 quality from Air Liquide) stripping measurements were recorded over a potential range from 0.05 to 1.00 or 1.20 V *vs.* RHE at a potential scan rate of 0.02 V s^{-1}. CO stripping measurements are recorded after 30 min-chronoamperometry (CA) at 0.10 V *vs.* RHE in a CO saturated electrolyte (5 min) followed by N_2-bubbling for 25 min to remove dissolved CO. CO stripping measurements in presence of H_2 (H2 HG quality from Air Liquide) are recorded at a rotation rate of 1,600 rpm after a 30 min-chronoamperometry at 0.10 V *vs.* RHE in a CO saturated electrolyte (5 min) followed by N_2-bubbling for 15 min to remove dissolved CO, and H_2-bubbling for 10 min to saturate the electrolyte. HOR polarization curves are recorded in a H_2-saturated electrolyte at a potential scan rate of 0.005 V s^{-1} and different electrode rotation rates.

3. Results and discussion

3.1. Physicochemical characterisation of the materials

First, TGA analyses were performed to check the metal loadings on the carbon support; values ranging from 37 wt% to 39 wt%, i.e., very close to the targeted one (40 wt%), were obtained. ICP-OES analyses indicated that the bulk compositions of materials were also very close to the nominal ones (Table 1). Both these results put together indicate that the synthesis reactions have occurred quantitatively. Further, mass activity of catalysts was determined taking into account these characterisations.

X-ray diffractograms were recorded to obtain information on the phases composing the catalysts (Fig. 1). All XRD patterns display a peak at 2 θ ≈ 25° attributed to the (002) planes of turbostratic graphite in Vulcan XC 72 carbon [30] and peaks at 2θ of *ca.* 39.8°, 46.4°, 67.6° and 81.4° assigned to (111), (200), (220) and (311) planes of the face-centred cubic (fcc) structure of Pt (JCPDS card n°. 04–0802) [31], respectively. For tin containing catalysts, additional peaks appear and grow in intensity as the tin content increases. These peaks located at *ca.* 26.4°, 34.1° and 51.8° correspond to the (110), (101) and (211) planes of a SnO_2 phase having a tetragonal rutile structure (JCPDS card n°. 41–1445)[32,33], respectively. Moreover, the diffraction peaks assigned to Pt are shifted towards lower 2θ values, which can be due to the formation of an alloy between Pt and Sn. Indeed, the incorporation of Sn into the Pt lattice should result in an increase of the interplanar spacing and therefore in a shift of the diffraction peaks towards lower 2θ values [34]. The crystallite sizes and the corresponding lattice parameters have been calculated from the Pt (1 1 1) diffraction peak using the Debye-Scherrer formula and the Bragg equation (Table 1), respectively. The lattice parameter values are higher for the bimetallic materials than for the monometallic Pt/C catalyst, leading to low degrees of alloying from *ca.* 5 % to *ca.* 8 % as the tin content in catalysts increases.

Table 1
Physicochemical characterisation of the Pt-based catalysts: metal weight loadings by TGA, bulk atomic composition by ICP-OES, crystallite size (L_v) and cell parameter (a) by XRD and particle size (d_{TEM}) by TEM.

	Metal wt.%	Comp. at%	L_v (nm)	d_{TEM}	a_{cell} (nm)
Pt/C	37	100	2.5	2.1	3.92
$Pt_{90}(SnO_2)_{10}/C$	39	91/9	1.9	2.0	3.97
$Pt_{65}(SnO_2)_{35}/C$	39	61/39	2.5	2.6	3.97
$Pt_{50}(SnO_2)_{50}/C$	38	51/49	1.8	1.7	3.98

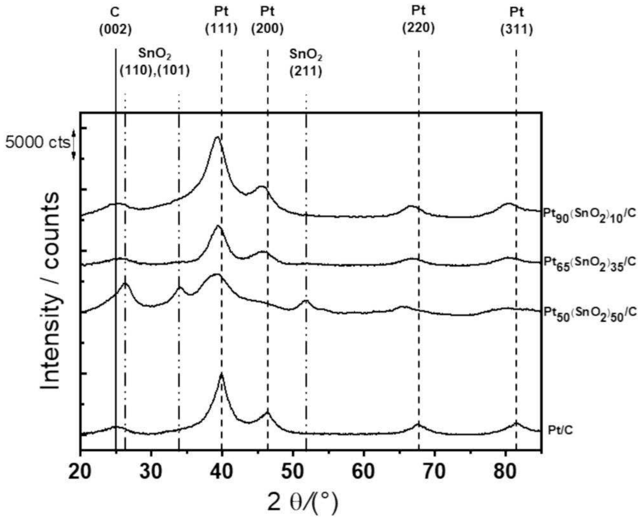

Fig. 1. XRD patterns of the Pt-based catalysts and peak assignation for the face centred cubic and hexagonal structures of Pt and SnO_2 according to the JCPDS 04–0802 and JCPDS 41–1445 cards, respectively.

TEM images of catalysts in Fig. 2 A, B, C and D show metal particles with small sizes well dispersed on the carbon support. However, according to the difference of contrast, it seems that two morphologies are deposited on the carbon support for tin-containing catalysts: isolated spherical nanoparticles with diameter close to 2 nm as determined from the histograms in Fig. 2 E, F, G and H, and agglomerate of 4–6 nm in size. EDS mappings (Fig. 2I, J and K) show that Pt and Sn are homogeneously distributed on the support. Their signals are superimposed, indicating that both metals are close each to the other. Energy filtered selected area electron diffraction patterns are displayed in Fig. 2 L. For the monometallic Pt/C catalysts, the ring sequence is characteristic of the fcc (Fm3m) structure of Pt. For the $Pt_{50}(SnO_2)_{50}/C$, additional rings appear, which could be assigned to the P4/4mnm tetragonal crystal structure of SnO_2.

XPS measurements were performed to determine the oxidation states of surface Pt and Sn atoms and possible electronic interactions between both metals. Considering the binding energy (BE) values in the Pt 4f orbital core spectra (Fig. 3 A, B, C and D), the fits of the spectra indicate that Pt is in all cases mainly present at the zero valent state (Pt^0 at BEs of *ca.* 71.2 and *ca.* 74.5 eV, for 4f 7/2 and 4f 5/2, respectively)[35,36], then at the + 2 valent state (PtO or $Pt(OH)_2$ at BEs of *ca.* 72.0 and 75.3 eV) and as trace amount at the four valent state (PtO_2 at BEs of *ca.* 75.2 eV and 78.5 eV) [37]. The ratio of Pt species varies between the catalysts, but no trend is observed, and the variation could be only due to exposure of catalyst to air (*ex situ* XPS analyses). It is also worth to note that the peak position seems to not shift with the tin atomic ratio in the catalysts (Fig. 3 E), as if no interaction between both Pt(PtSn) and SnO_2 occurred.

Now considering the Sn 3d orbital core spectra (Fig. 4), the fit of the signal indicates that for $Pt_{90}(SnO_2)_{10}/C$ (Fig. 4A) and $Pt_{65}(SnO_2)/C$ (Fig. 4B), Sn is present at different oxidation states leading to 3d 5/2 and 3d 3/2 peaks at BEs of *ca.* 485.4 eV and 493.8 eV, and *ca.* 487.2 eV and 495.6 eV, respectively. The BE value of the Sn 3d5/2 at *ca.* 485.4 eV is higher than that recorded for the pure Sn metal under the same conditions on our XPS apparatus (485.0 eV). It is close to that obtained by Wang et al. [38] on PtSn bimetallic nanoparticles (485.6 eV). These authors noted that such a value was higher than those usually reported in the literature for metallic Sn (485.0 eV) [35,39] but lower than values typically reported for oxidic Sn species (485.8 eV to 487.0 eV) [38]. Based on studies on surface alloying at the Sn-Pt(111) interface, Galeotti et al. [40] have shown that alloying induced a shift by *ca.* 0.3 eV towards higher BE with respect to the same peaks for bulk Sn. A BE value of 485.3 eV was also assigned to the formation of a PtSn alloy by Virnovskaia et al. [41]. The formation of an alloy, even at a low degree, has been evidenced by XRD measurements. But the partial oxidation of Sn at

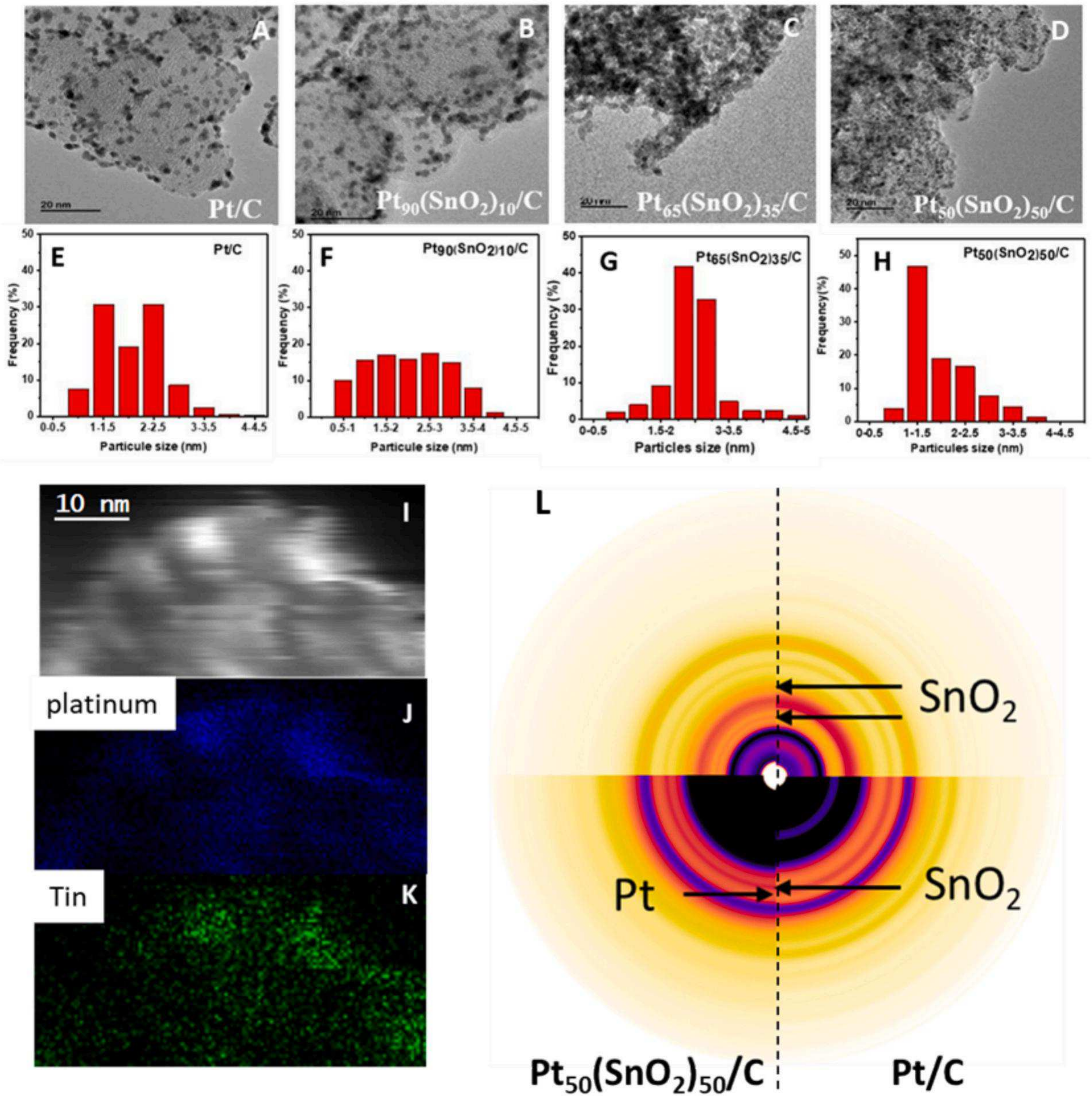

Fig. 2. (A, B, C, and D) TEM images of the Pt-based catalysts, (E, F, G, H) corresponding size distribution histograms for isolated NPs, (I, J, K) EDS mapping of the $Pt_{50}(SnO_2)_{50}/C$ catalyst and (L) EF-SAED analyses of the carbon support, Pt/C and $Pt_{50}(SnO_2)_{50}/C$ catalysts.

the surface of Pt nanoparticles can also occurs and the BE value recorded can represent the average of at least both these processes [38]. The Sn 3d5/2 peak at higher BE (between 486.9 eV and 487.4 eV) is certainly due to the presence of a highly oxidized phase [37], and a SnO_2 structure has been identified by both XRD and EF-SAED measurements. The position of these peaks is shifted towards lower BE values compared to that for the pure SnO_2/C material (Fig. 4 D), and the delta increases with the ratio of SnO_2 in the catalyst (Fig. 4 E), which could again translate into an electron transfer from Pt and/or PtSn towards SnO_2 [42,43]. This electron transfer does not produce any observable BE shift for Pt (Fig. 3E). Such phenomenon was already observed by Ma et al. for Pt_xSe_x [44] and by Babu et al. [45] for Ru_xSe_y materials, where the BE values for Se 3d shifted towards lower values while those of Pt 4f or Ru 3d remained unchanged, which was proposed to be due to the open d-shell configuration of Pt or Ru. This electron transfer could explain the higher BE values for Sn^0 than that generally obtained from the literature and the lower one for SnO_2 in Sn-containing catalysts than in the pure SnO_2/C material, as well as the decrease of the intensity of the Sn^0 peak with respect to that at higher BE (between 486.9 eV and 487.4 eV), to completely disappear for the $Pt_{50}Sn_{50}/C$ catalyst (Fig. 4C); indeed, as the amount of Sn increases in the catalysts, the alloying degree remains low but the formation of highly oxidized tin species increases).

From this comprehensive characterisation of the catalysts, $Pt(SnO_2)/C$ materials correspond to slightly alloyed PtSn (5 % to 8 %) nanoparticles of *ca.* 2 nm mean diameter in strong interaction with a SnO_2 structure, allowing an electronic metal support interaction (EMSI) [43,46]. Indeed, physicochemical characterization of the catalysts indicates clearly the existence of metallic Pt and of SnO_2, and also that Pt and SnO_2 are localized at the same place, which will favour interactions between those species.

3.2. *Electrochemical characterisation of catalysts*

CVs were recorded in a N_2-purged 0.1 M $HClO_4$ aqueous electrolyte at 0.02 V s^{-1} and 25 °C (Fig. 5A). The CVs show a decrease of current in the $H_{UPD/desorption}$ (hydrogen underpotential deposition/desorption)

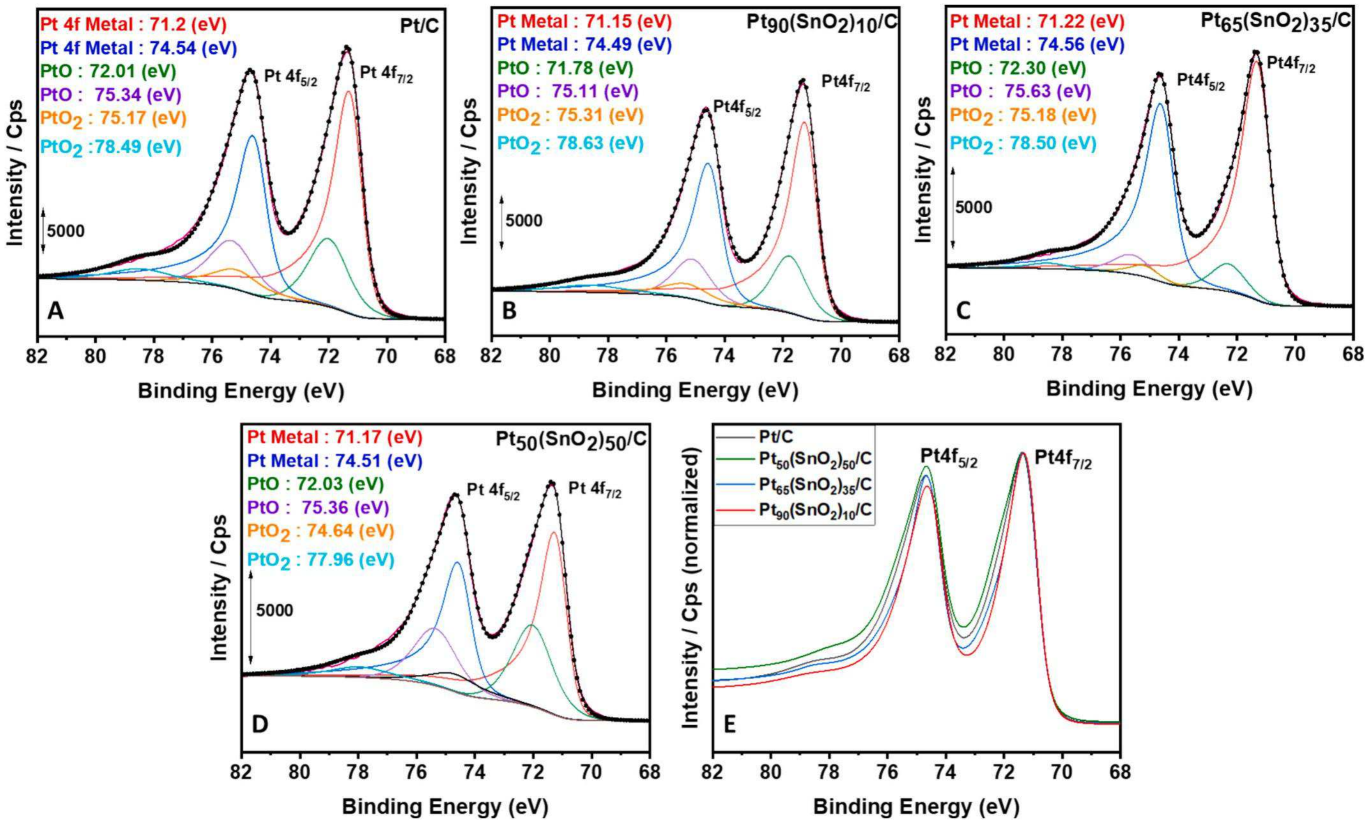

Fig. 3. XPS core level spectra of Pt 4f recorded on (A) Pt/C, (B) $Pt_{90}(SnO_2)_{10}/C$, (C) $Pt_{65}(SnO_2)_{35}/C$, (D) $Pt_{50}(SnO_2)_{50}/C$ catalysts (each component used to fit the spectra are presented with the corresponding legend) and (E) comparison of the XPS core level spectra of Pt 4f recorded for all the catalysts.

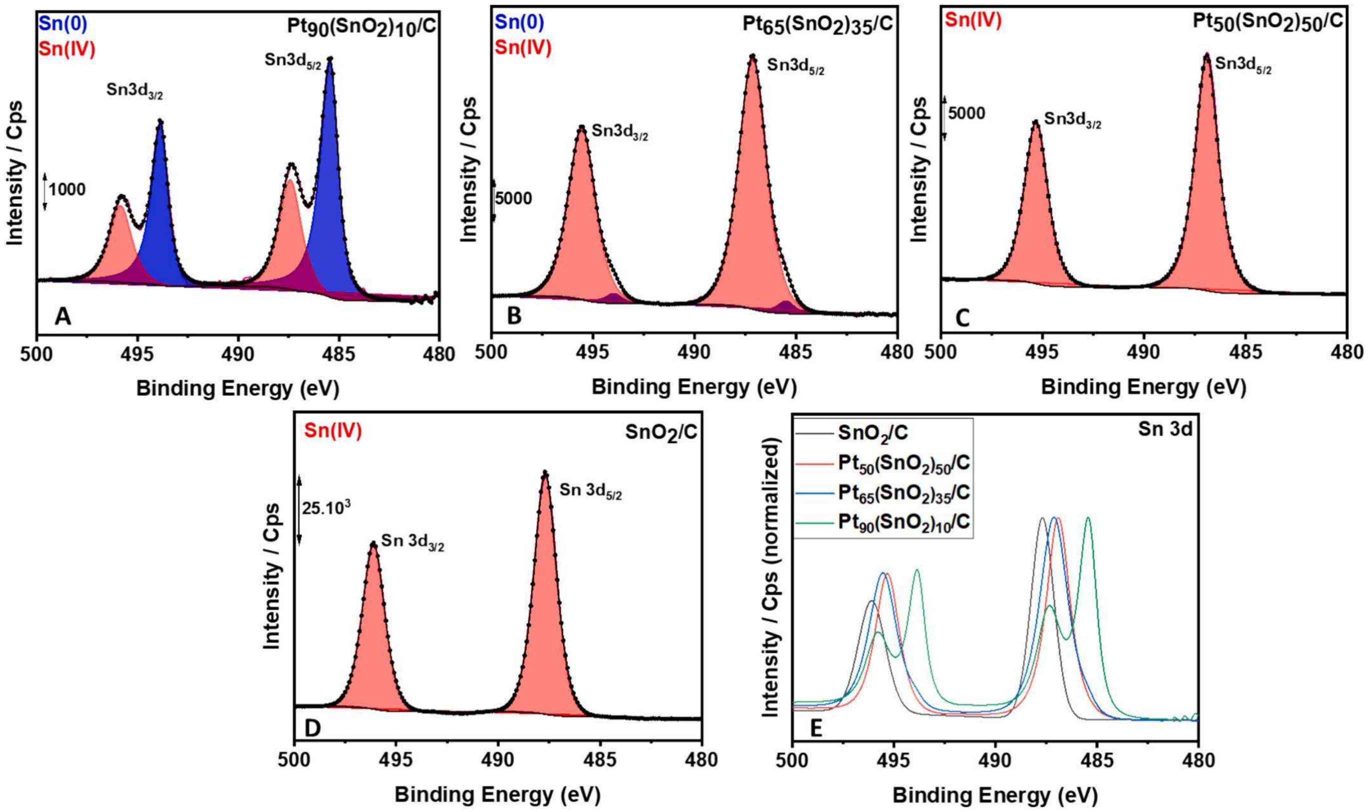

Fig. 4. XPS core level spectra of Sn 3d recorded on (A) SnO_2/C, (B) $Pt_{90}(SnO_2)_{10}/C$, (C) $Pt_{65}(SnO_2)_{35}/C$, (D) $Pt_{50}(SnO_2)_{50}/C$ catalysts (each component used to fit the spectra are presented with the corresponding legend) and (E) comparison of the XPS core level spectra of Sn 3d recorded for all the catalysts.

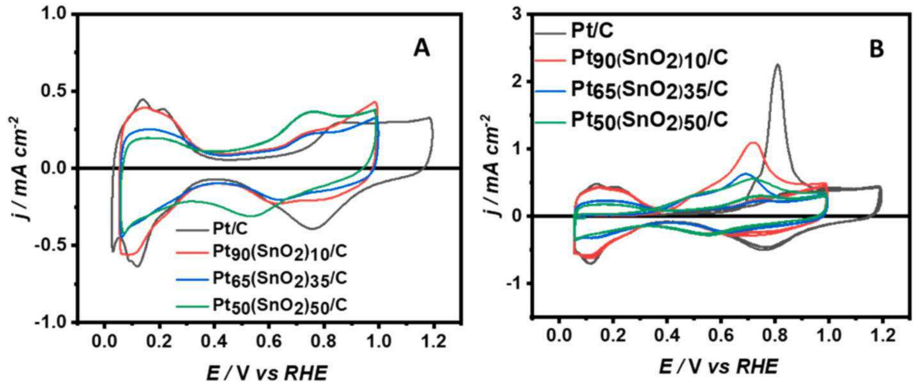

Fig. 5. (A) Cyclic voltammograms of Pt-based catalysts in N_2-purged 0.1 mol L^{-1} $HClO_4$ electrolyte, (B) CO stripping voltammograms on the Pt-based catalysts in N_2-purged 0.1 mol L^{-1} $HClO_4$ electrolyte after CO adsorption for 5 min at 0.10 V *vs.* RHE (scan rate = 0.02 V s^{-1}, $T = 25$ °C and electrode rotation rates, $\omega = 1600$ rpm).

potential region on Pt (between 0.05 V and 0.40 V *vs.* RHE) and an increase of the capacitive current between 0.40 V and 0.50 V *vs.* RHE with the increasing SnO_2 content. These behaviours indicate that the surface of platinum is covered by tin, most likely under the form of a SnO_2 phase, as it is known to be a good capacitive material [47]. The electroactive surface area of the catalysts has been assessed from the H_{UPD} region ($EASA_{HUPD}$) after correction of the capacitive double layer current density [48]. $EASA_{HUPD}$ values in Table 2 confirm the decrease of surface Pt availability with the increase of tin content in catalysts.

The CO stripping profile recorded on Pt/C (Fig. 5B) is typical of a material synthesized by the polyol method [49–51], displaying an apparent onset potential of oxidation at *ca.* 0.65 V *vs.* RHE, followed by a shoulder and the main peak centred at *ca.* 0.80 V *vs.* RHE. The assignation of the different features can be found in our previous work [51]. The CO stripping profiles of tin-containing materials show two peaks, one with a maximum close to 0.50 V *vs.* RHE and the other one with a maximum in the 0.70 V – 0.80 V *vs.* RHE range (depending on the tin ratio), in agreement with previous studies on PtSn catalysts [36,52]. The charge involved for the removal of CO decreases from 50.5 C for Pt/C to 37.7 C for $Pt_{50}(SnO_2)_{50}$/C, confirming the lower availability of Pt surface as the ratio of tin in the catalyst increases. Also, the onset potential dramatically shifted toward lower values. From *in situ* infrared spectroscopy measurements of CO oxidation on Pt_3Sn(hkl) surfaces, Stamenković et al. [53] proposed two different forms of adsorbed CO on Pt_3Sn(111), with different reactivity, but did not observe the same behaviour on Pt_3Sn(100). Moreover, other authors studying CO oxidation on PtSn nanoparticles supported on carbon [54] did not obtain any evidence of different adsorbed CO by *in situ* infrared spectroscopy, nor of a ligand effect. They proposed then that the bifunctional mechanism was the main oxidation process at low potential. However, here the oxidation onset potential decreases from 0.28 V *vs.* RHE for the $Pt_{90}(SnO_2)_{10}$/C catalyst to 0.22 V *vs.* RHE for the $Pt_{50}(SnO_2)_{50}$/C one. This is an important observation, because Huang et al. [52] have shown using *in situ* XAS (x-ray absorption spectroscopy) measurements that in addition to a bifunctional mechanism involving the Pt-Sn/Pt-Sn-OH redox couple at low potentials, the change of the onset potential for the CO oxidation with the Sn coverage indicated that the CO oxidation could be promoted by weakening Pt-CO bond through a Ligand effect involving both strong Pt-Sn bonds and interaction between Pt-CO and Sn-OH co-adsorbed species.

The decrease in Pt surface availability with the increase of the tin ratio in catalysts could be detrimental for their electrocatalytic activity towards the HOR. Then HOR polarization curves were recorded at different rotation rates in a H_2-saturated 0.1 M $HClO_4$ aqueous electrolyte at 0.005 V s^{-1} and 298 K (Fig. 6 A, D, G and J), from which the corresponding Koutecky-Levich plots were drawn (Figures B, E, H and K).

Kinetic parameters such as the kinetic current density (j_k), exchange current density ($j_\circ$) and Tafel slope (b) are then determined by using the generalized Koutecky-Levich equation [12,49]. Tafel plots are given in Fig. 6 C, F, I and L. Table 2 gives the values of the kinetic parameters obtained for all the materials.

$$\frac{1}{j} = \frac{1}{j_l^{\text{diff, elec}}} + \frac{1}{j_l^{\text{film}}} + \frac{1}{j_k} = \frac{1}{j_l^{\text{diff, elec}}} + \frac{1}{j_l^{\text{film}}} + \frac{1}{j_\circ e^{\eta/b}} \qquad (2)$$

where j is the current density at a given electrode potential, $j_l^{\text{diff, elec}}$ the diffusion limiting current density of H_2 in the electrolyte, j_l^{film} the diffusion limiting current density in the catalytic film, and η is the HOR overpotential.

The $j_\circ$ and j_k values are all very close to that determined for the pure Pt/C catalyst, although the EASA are much lower, particularly in the case of the $Pt_{50}(SnO_2)_{50}$/C catalyst. Indeed, the catalyst mass activity (MA) and specific activity (SA) dramatically increase with the increase of tin content, by factors two and four, respectively. It is well known that SnO_2 is not active for the HOR, but its interaction with Pt or PtSn seems to induce a modification of the electronic state of the Pt or PtSn surface active sites (EMSI), which accelerates the HOR kinetics. It is generally proposed an electron transfer from the metal oxide toward Pt to explain the SMSI effect [22,23]. It is worth noting that the same electron transfer, i.e., from the metal oxide toward Pt, is evoked for the enhancement of both the ORR [22] and the HOR[55]. Shen et al.[55]

Table 2
Electroactive surface area ($EASA_{HUPD}$) and kinetic data for the HOR assessed from rotating disc electrode measurements in Fig. 6 at Pt-based catalysts: kinetic current density (j_k), specific activity (SA) and mass activity (MA) at 0.02 V *vs.* RHE, and exchange current density (j_o) and Tafel slope (b).

	Pt/C	**$Pt_{90}(SnO_2)_{10}$/C**	**$Pt_{65}(SnO_2)_{35}$/C**	**$Pt_{50}(SnO_2)_{50}$/C**	**Pt/C Tanaka**	**$Pt_{60}Ru_{40}$/C Tanaka**
$EASA_{HUPD}$ (m^2 g_{Pt}^{-1})	50.1	49.7	27.6	20.5	99.9	48.3
j_k (mA cm^{-2})	6.3	6.2	5.6	5.8	4.4	2.3
SA (mA cm_{Pt}^{-2})	0.33	0.30	0.63	1.33	0.10	0.18
MA (mA mg_{Pt}^{-1})	147	151	211	286	101	88
$j_\circ$ (mA cm^{-2})	1.37	1.40	1.25	1.30	1.15	1.24
b (mV dec^{-1})	28	30	29	28	31	34

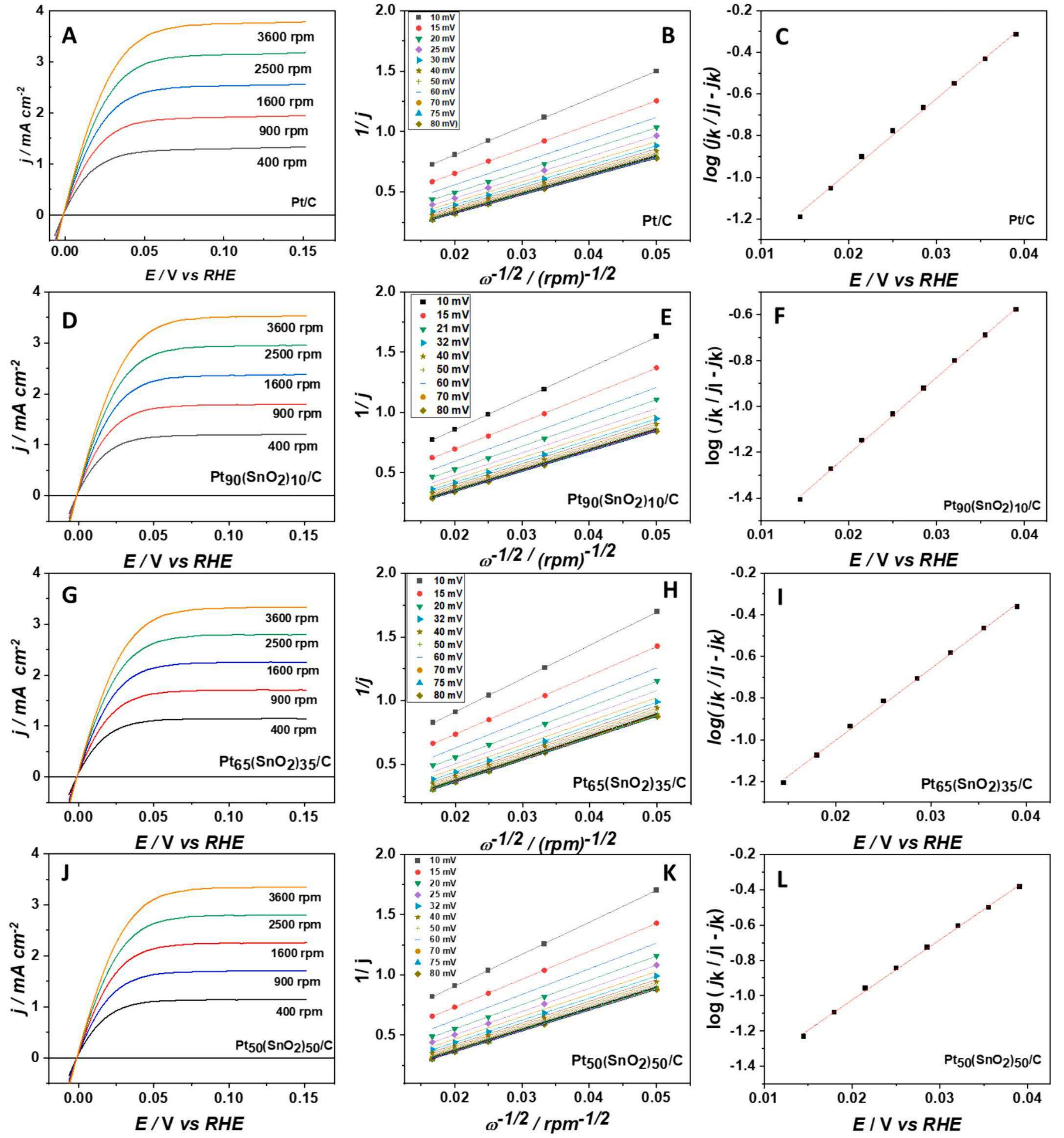

Fig. 6. (A, D, G, J) Hydrodynamic polarization curves recorded at a scan rate = 0.005 V s^{-1} and T = 25 °C in H_2-saturated 0.1 mol L^{-1} $HClO_4$ electrolyte on the Pt based catalysts at different electrode rotation rates, (B, E, H, K) corresponding Koutecky-Levich straight lines determined at different potentials and derived Tafel plots (C, F, I, L).

explained that "the collaboration between tungsten oxide and tungsten carbide species could reduce the reliance on Pt while enhancing both the HOR activity and the anti-CO poisoning capability, by proposing an electron transfer from the metal oxide towards Pt, and cited Vayssilov et al. [56] who showed in their article the contrary, i.e. an electron transfer from Pt toward the tungsten oxide. Moreover, some authors identified electron transfer from the Pt nanoparticles toward the oxide support on Pt-ceria catalysts, and oxygen transfer from ceria to Pt [56], or from Ru toward SnO_2 for Ru-SnO_x/Al_2O_3 catalyst [57]. Recently, Chen et al. [58] have pointed out the role of the electronegativity of different catalytic materials (Fe, Ni, Ru, and Pt, with electronegativity values on the Pauling scale of 1.83, 1.91, 2.20 and 2.28, respectively) on the adsorption/activation of H_2: the higher is the electronegativity with respect to that of H (2.20 on the Pauling scale), the higher the adsorption of H under H^+ form.

Several mechanisms were proposed in the literature for the HOR, that leans on three fundamental steps, i.e., the Tafel step involving the dissociative adsorption of hydrogen on two catalytic sites, the Heyrovsky step involving the dissociative adsorption of H_2 on one catalytic site with one electron transfer and the Volmer step involving one electron transfer for the oxidation of adsorbed H into H^+. In acidic media, the HOR occurs generally through the Tafel-Volmer or Heyrovsky-Volmer mechanism (Table 3).

A slope of *ca.* 30 mV dec^{-1} in our cases could then reflect that the same Volmer-Tafel (with the Tafel step being the rate determining step) mechanism occurs for the HOR on all the catalysts [59,60]. The invariance of the Tafel slopes values and the increase of the specific activity could indeed indicate that the mechanism on $Pt_x(SnO_2)_{100-x}/C$ catalysts is independent on the tin oxide ratio. However, the surface areas determined from the H_{UPD} desorption charge for the SnO_2-containing catalysts are twice smaller than those obtained from CO stripping, with $ECSA_{CO}$ values (37.7 $m^2\ g^{-1}_{Pt}$ and 39.2 $m^2\ g^{-1}_{Pt}$ for $Pt_{50}(SnO_2)_{50}/C$ and $Pt_{65}(SnO_2)_{35}/C$, respectively). This indicates a very low H coverage of the surface which can be due to the fact that the adsorption of H_2 via a Tafel process would involve 2 adjacent Pt atoms, whereas that of linear CO would necessitate only one Pt site. It is then proposed that the hydrogen adsorption on SnO_2-containing catalysts occurs through the Heyrovsky mechanism. Indeed, microkinetic analysis of the HOR [60] showed that at low H surface coverage Tafel slopes lower than 120 mV dec^{-1} are only obtained considering the Heyrovsky-Volmer mechanism. In agreement with XPS results, we propose then that the electron transfer from Pt to SnO_x likely involves an increase of Pt electronegativity favouring the whole process of H_2 adsorption, dissociation and electron transfer to Pt (and electrode) in the Heyrovsky step. Jiang and co-workers [61] have evidenced an electron transfer from Ru to the N-doped graphite overlayers in Ru@NC/C and a lower d-band centre of Ru which could result in decreased binding energy of adsorbed species such as H and CO. Such explanation could also apply in our case for Pt explaining the activity and tolerance enhancement towards the HOR and CO_{ads}, respectively, with the increase of SnO_2 ratio.

Now that we have established that $Pt(SnO_2)/C$ catalysts display lower CO oxidation onset potentials in N_2-saturated electrolyte and higher activity towards the HOR in pure electrolyte than a Pt/C catalyst, it is important to check their behaviour toward the HOR in the presence of CO. Fig. 7A displays the CVs recorded at a scan rate of 0.02 V s^{-1} in a H_2-saturated 0.1 M $HClO_4$ electrolyte after surface saturation by CO, at a rotation rate of 1600 rpm and a temperature of 25 °C. Looking to the first positive linear potential variation on the Pt/C catalyst, no current is observed from 0.05 V *vs.* RHE to the onset potential for the HOR at *ca.* 0.40 V *vs.* RHE, indicating that the Pt surface is completely blocked by CO. The HOR onset potential is 300 mV lower than the apparent onset potential of CO stripping in N_2-purged electrolyte (Fig. 5B). This behaviour has already been explained in our previous work in terms of oxidation of a few CO_{ads} on certain Pt sites through an Eley-Rideal mechanism occurring at low potential and freeing very active Pt sites for the HOR [49].

The addition of SnO_2 to Pt reduces dramatically the overpotentials for the HOR confirming the effectiveness of metal oxide addition to improve catalytic performance in the presence of poisons such as CO. Also, as the proportion of SnO_2 increases, the overpotential decreases from *ca.* 0.28 V *vs.* RHE on $Pt_{90}(SnO_2)_{10}/C$ to *ca.* 0.21 V *vs.* RHE on $Pt_{50}(SnO_2)_{50}/C$, in agreement with results observed from CO stripping measurements (Fig. 5B), and confirming the proposition of Huang et al. [52] for the promotion of CO oxidation by weakening Pt-CO through a Ligand effect.

Table 3
HOR Mechanisms in acidic media. *corresponds to an adsorption site.

Mechanism	Rate determining step	Tafel slope
Tafel-Volmer	$H_2 + 2\ * \rightarrow 2\ H_{ads}$ Tafel	30 mV dec^{-1}
Tafel-Volmer	$H_{ads} \rightarrow * + H^+ + e^-$ Volmer	60 mV dec^{-1}
Heyrovsky-Volmer	$H_2 + * \rightarrow H_{ads} + H^+ + e^-$ Heyrovsky	40 mV dec^{-1}
Heyrovsky-Volmer	$H_{ads} \rightarrow * + H^+ + e$- Volmer	120 mV dec^{-1}

At last, the positive effect of the presence of SnO_x was assessed at 60 °C (Fig. 7), a temperature closer to that of PEMFC working conditions, for which the solubility in water of both H_2 and CO remains acceptable (dropping down from *ca.* 0.00155 g/kg at 25 °C to 0.00118 g/kg at 60 °C for H_2, i.e., a 24 % loss, and from *ca.* 0.025 g/kg at 25 °C to 0.015 g/kg at 60 °C for CO, i.e., a 40 % loss) [62]. Fig. 7 B displays the two first CVs of CO_{ads} stripping on the Pt/C catalyst at 25 °C and 60 °C. Both sets of CVs display the same features, but the CO_{ads} oxidation onset potential and the main oxidation peak are shifted towards lower potentials at 60 °C. This behaviour seems to indicate that the water activation to form adsorbed OH is favoured by the temperature on Pt/C catalyst, which allows the Langmuir-Hinshelwood mechanism occurring at lower potentials. Now, considering the $Pt_x(SnO_2)_{100-x}/C$ catalysts in Fig. 7 D, the CO_{ads} oxidation onset potentials recorded at 60 °C are same as those recorded at 25 °C; only the position of the main peak is shifted towards lower values. This seems to indicate that the ligand effect is not promoted by temperature, but that the activation of water at SnO_2 containing species is. However, in the presence of hydrogen, all electrodes display an oxidation current from 0.05 V *vs.* RHE at 60 °C, which indicates that the Pt surfaces were not completely blocked by CO_{ads} after the CA in CO-saturated electrolyte. This could be due to the solubility decrease of CO with temperature, but this hypothesis doesn't explain either the higher HOR current densities recorded on $Pt_x(SnO_2)_{100-x}/C$ catalysts at low potentials than on Pt/C, nor the absence of H_{UPD} feature between 0.05 V and 0.40 V *vs.* RHE. It seems then that few Pt sites are not blocked, allowing the HOR at low potential (between 0.05 and 0.30 V *vs.* RHE) and that the presence of SnO_2 species enhances the rate of the HOR, likely through a EMSI effect at so low potentials. Indeed, the Pt surface availability is lower for $Pt_x(SnO_2)_{100-x}/C$ catalysts than for Pt/C catalyst as evidenced by the second cycle recorded after CO stripping in Fig. 7 B and C, where the charges in the H_{UPD} region are lower. For potential higher than 0.2 V *vs.* RHE, the slope of the oxidation wave increases, and the order of activity between the catalysts is the same as in Fig. 7A. From this potential, the bifunctional mechanism occurs, as well as the Ligand effect. Under these conditions, the $Pt_{50}(SnO_2)_{50}/C$ displays the best activity towards the HOR at low potential and the higher tolerance toward the presence of CO.

4. Conclusion

Carbon-supported platinum-tin oxide catalysts with different compositions $(Pt_{100-x}(SnO_2)_x/C$ were synthesized by a conventional polyol process. Physicochemical characterisations (TGA, ICP-MS, XRD, TEM, HR-TEM, SEAD) revealed the formation of $Pt(SnO_2)/C$ materials with metal ratio close and composition close to the nominal ones, and corresponding to slightly alloyed PtSn (5 % to 8 %) nanoparticles (mean particles sizes from 1.5 − 2.5 nm) in strong interaction with a SnO_2 structure, allowing an electronic metal support interaction (EMSI). Indeed, XPS measurements indicated clearly an electron transfer from Pt/PtSn nanoparticles towards SnO_2. Electrochemical characterisation showed activity enhancement by a factor two for the mass activity and a factor four for the specific activity towards the HOR for the SnO_2-containing catalysts, which was attributed to an EMSI effect involving a change of the Pt electronegativity. A higher tolerance towards CO poisoning than on pure Pt/C was also observed, in both cases the absence and the presence of H_2. The shift of the onset potential towards lower values with the increase of tin content is explained in terms of a ligand effect decreasing the Pt-CO bond strength. which allows the bifunctional mechanism in the presence of SnO_2 to start also at lower potentials.

Overall, $Pt_{50}(SnO_2)_{50}/C$ catalyst seems to be the best compromise: (i)

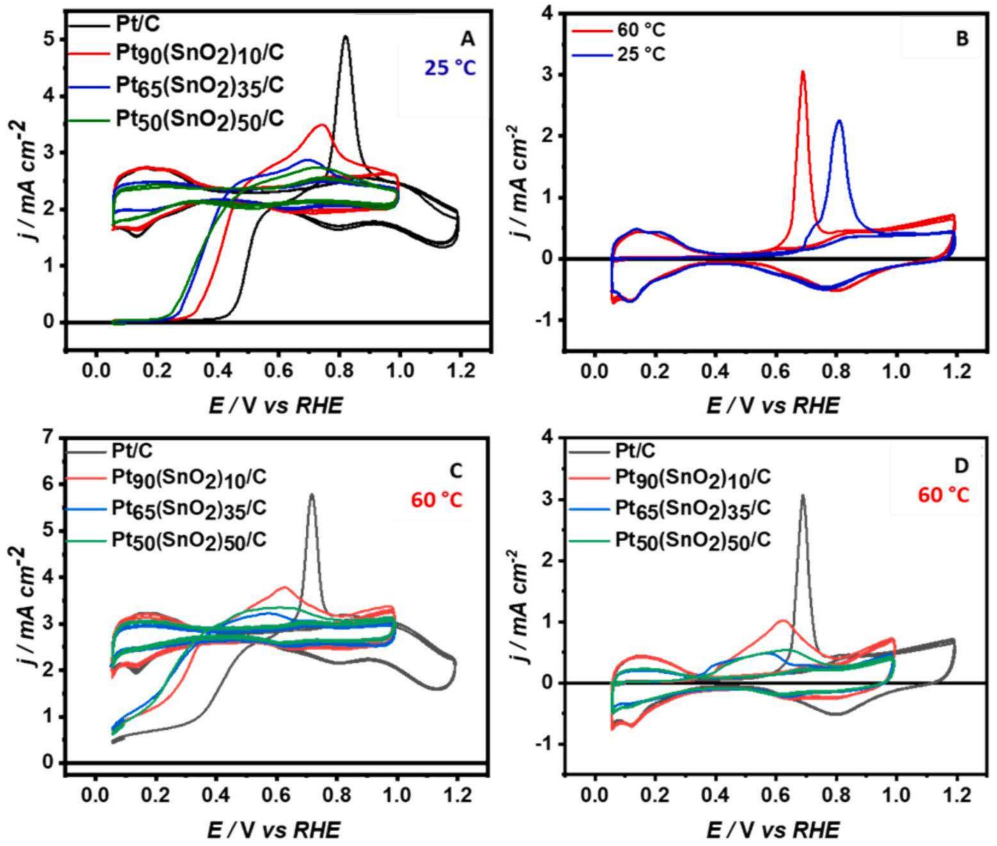

Fig. 7. (A) Cyclic voltammograms of the $Pt_x(SnO_2)_{100-x}/C$ catalysts recorded at 25 °C in H_2-purged 0.1 mol L^{-1} $HClO_4$ electrolyte after CO adsorption for 5 min at 0.10 V *vs.* RHE; (B) Cyclic voltammograms of Pt/C catalysts recorded at 25 °C and 60 °C in N_2-purged 0.1 mol L^{-1} $HClO_4$ electrolyte after CO adsorption for 5 min at 0.10 V *vs.* RHE; (C) Cyclic voltammograms recorded of the $Pt_x(SnO_2)_{100-x}/C$ catalysts recorded at 60 °C in H_2-purged 0.1 mol L^{-1} $HClO_4$ electrolyte after CO adsorption for 5 min at 0.10 V *vs.* RHE; (D) Cyclic voltammograms of $Pt_x(SnO_2)_{100-x}/C$ catalysts recorded at 25 °C in N_2-purged 0.1 mol L^{-1} $HClO_4$ electrolyte after CO adsorption for 5 min at 0.10 V *vs.* RHE. (Scan rate = 0.020 V s^{-1}, ω = 1600 rpm).

it displays a high electrocatalytic activity for HOR, (ii) hence, it helps reducing the atomic quantity of Pt by a half in the catalyst, which allows for reducing the production costs of fuel cell anode materials, (iii), it allows removing CO_{ads} from the low potentials of *ca.* 0.2 V and 0.05 V *vs.* RHE at 20 °C and 60 °C, respectively, (iv) hence, it possesses an activity for the HOR from 0.2 V and 0.05 V *vs.* RHE in the presence of CO at 20 °C and 60 °C, respectively, and (v) it allows feeding the fuel cell with less pure (and then less costly) hydrogen.

CRediT authorship contribution statement

Franck Koffi Bouho: Writing – review & editing, Writing – original draft, Investigation. **Weliton Silva Fonseca:** Writing – review & editing, Writing – original draft, Investigation. **Sirine Ben Latifa:** Writing – review & editing, Writing – original draft, Investigation. **Thibault Rafaïdeen:** Writing – review & editing, Writing – original draft, Methodology, Investigation, Formal analysis, Conceptualization. **Frédéric Pailloux:** . **Julie Rousseau:** Writing – review & editing, Writing – original draft, Formal analysis. **Christine Canaff:** Writing – review & editing, Writing – original draft, Investigation, Formal analysis. **Sophie Morisset:** Writing – review & editing, Writing – original draft, Investigation, Formal analysis. **Têko W. Napporn:** Writing – review & editing, Writing – original draft, Validation, Resources, Methodology, Investigation, Conceptualization. **Christophe Coutanceau:** Writing – review & editing, Writing – original draft, Validation, Supervision, Resources, Project administration, Methodology, Funding acquisition, Formal analysis, Conceptualization.

Declaration of competing interest

The authors declare that they have no known competing financial interests or personal relationships that could have appeared to influence the work reported in this paper.

Acknowledgements

This work was performed in the framework of the PEMFC95 project funded by the “France 2030” government investment plan managed by the French Research Agency, under the reference “ANR-22-PEHY-0005”. The authors also acknowledge financial support from the European Union (ERDF) and Région Nouvelle Aquitaine. This work pertains to the French government program “Investissements d’Avenir” (EUR INTREE, reference ANR-18-EURE-0010).

Data availability

Data will be made available on request.

References

[1] D. Panarello, A. Gatto, Decarbonising Europe – EU citizens’ perception of renewable energy transition amidst the European Green Deal, Energy Policy 172 (2023) 113272, https://doi.org/10.1016/j.enpol.2022.113272.

[2] O.A. Shobande, A.K. Tiwari, L. Ogbeifun, N. Trabelsi, Demystifying circular economy and inclusive green growth for promoting energy transition and carbon neutrality in Europe, Struct. Change Econ. Dyn. 70 (2024) 666–681, https://doi.org/10.1016/j.strueco.2024.05.016.

[3] I.K. Ofori, E.Y. Gbolonyo, N. Ojong, Foreign direct investment and inclusive green growth in Africa: Energy efficiency contingencies and thresholds, Energy Econ. 117 (2023) 106414, https://doi.org/10.1016/j.eneco.2022.106414.

[4] V.A. Sethuraman A.Z. Weber J.W. Weidner Fuel Cells – Proton-Exchange Membrane fuel Cells J. Garche Encyclopedia of Electrochemical Power Sources 2009 Elesevier, Amsterdam 817 827 10.1016/B978-044452745-5.00228-8.

[5] X. Yu, S. Ye, Recent advances in activity and durability enhancement of Pt/C catalytic cathode in PEMFC: Part I. Physico-chemical and electronic interaction between Pt and carbon support, and activity enhancement of Pt/C catalyst, J. Power Sources 172 (2007) 133–144, https://doi.org/10.1016/j.jpowsour.2007.07.049.

[6] H. A. Gasteiger, J. E. Panels, S. G. Yan, Dependence of PEM fuel cell performance on catalyst loading, J. Power Sources 127 (2004) 162–171, https://doi.org/10.1016/j.jpowsour.2003.09.013.

[7] R.J. Bellows, E.P. Marucchi-Soos, D.T. Buckley, Analysis of Reaction Kinetics for Carbon Monoxide and Carbon Dioxide on Polycrystalline platinum Relative to fuel Cell operation, Ind. Eng. Chem. Res. 35 (1996) 1235–1242, https://doi.org/10.1021/ie950580m.

[8] N. Rajalakshmi, T.T. Jayanth, K.S. Dhathathreyan, Effect of Carbon Dioxide and Ammonia on Polymer Electrolyte Membrane fuel Cell Stack Performance, Fuel Cells 3 (2003) 177–180, https://doi.org/10.1002/fuce.200330107.

[9] W.A. Adams, J. Blair, K.R. Bullock, C.L. Gardner, Enhancement of the performance and reliability of CO poisoned PEM fuel cells, J. Power Sources 145 (2005) 55–61, https://doi.org/10.1016/j.jpowsour.2004.12.049.

[10] T. Lopes, V.A. Paganin, E.R. Gonzalez, The effects of hydrogen sulfide on the polymer electrolyte membrane fuel cell anode catalyst: H_2S–Pt/C interaction products, J. Power Sources 196 (2011) 6256–6263, https://doi.org/10.1016/j.jpowsour.2011.04.017.

[11] D.C. Papageorgopoulos, F.A. de Bruijn, Examining a potential fuel Cell Poison : a Voltammetry Study of the Influence of Carbon Dioxide on the Hydrogen Oxidation Capability of Carbon-Supported Pt and PtRu Anodes, J. Electrochem. Soc. 149 (2001) A140, https://doi.org/10.1149/1.1430413.

[12] M.J. Croissant, T. Napporn, J.M. Léger, C. Lamy, Electrocatalytic oxidation of hydrogen at platinum-modified polyaniline electrodes, Electrochim. Acta 43 (1998) 2447–2457, https://doi.org/10.1016/0013-4686(96)00127-2.

[13] A. Hassan, A. Carreras, J. Trincavelli, E.A. Ticianelli, Effect of heat treatment on the activity and stability of carbon supported PtMo alloy electrocatalysts for hydrogen oxidation in proton exchange membrane fuel cells, J. Power Sources 247 (2014) 712–720, https://doi.org/10.1016/j.jpowsour.2013.08.138.

[14] J. Asgardi, J.C. Calderón, F. Alcaide, A. Querejeta, L. Calvillo, M.J. Lázaro, G. García, E. Pastor, Carbon monoxide and ethanol oxidation on PtSn supported catalysts: effect of the nature of the carbon support and Pt:Sn composition, Appl. Catal. B: Environ. 168–169 (2015) 33–41.

[15] N. Narischat, T. Takeguchi, T. Mori, S. Iwamura, I. Ogino, S. Mukai, W. Ueda, Effect of the mesopores of carbon supports on the CO tolerance of Pt_2Ru_3 polymer electrolyte fuel cell anode catalyst, Int. J. Hydrog. Energy 41 (2016) 13697–13704, https://doi.org/10.1016/j.ijhydene.2016.05.272.

[16] M. Gonzalez-Hernandez, E. Antolini, J. Perez, CO tolerance and stability of PtRu and PtRuMo electrocatalysts supported on N-doped graphene nanoplatelets for polymer electrolyte membrane fuel cells, Int. J. Hydrog. Energy 45 (2020) 5276–5284, https://doi.org/10.1016/j.ijhydene.2019.05.208.

[17] C. Coutanceau, S. Baranton, C. Lamy, Determination of reaction mechanisms occurring at electrocatalysts using electrochemical methods, spectroelectrochemical measurements and analytical techniques, in: P. Balbuena, V. Subramanian (Eds.), Modern Aspects of Electrochemistry, Theory and Experiment in Electrocatalysis, Springer Science+Business Media, New Youk, 2010, pp. 397–501, https://doi.org/10.1007/978-1-4419-5594-4_10.

[18] P. Liu, A. Logadottir, J.K. Nørskov, Modeling the electro-oxidation of CO and H_2/CO on Pt, Ru, PtRu and Pt_3Sn, Electrochim. Acta 48 (2003) 3731–3742, https://doi.org/10.1016/S0013-4686(03)00538-3.

[19] A. Soussi, R. Haounati, Ait hssi, M. Taoufiq, S. Baoubih, Z. Jellil, S. El hankari, A. Elfanaoui, R. Markazi, A. Ihlal., Investigating structural, morphological, electronic, and optical properties of SnO_2 and Al-doped SnO_2: a combined DFT calculation and experimental study, Physica B: Cond. Matter 690 (2024) 416242, https://doi.org/10.1016/j.physb.2024.416242.

[20] P. Zhang, S.-Y. Huang, B.N. Popov, Mesoporous Tin Oxide as an Oxidation-Resistant Catalyst support for Proton Exchange Membrane fuel Cells, J. Electrochem. Soc. 157 (2010) B1163, https://doi.org/10.1149/1.3442371.

[21] M. Dou, M. Hou, D. Liang, W. Lu a, Z. Shao, B. Yi,, SnO_2 nanocluster supported Pt catalyst with high stability for proton exchange membrane fuel cells, Electrochim. Acta 92 (2013) 468–473, https://doi.org/10.1016/j.electacta.2013.01.070.

[22] H. Min, J.-H. Choi, H.E. Kang, D.J. Kim, Y.S. Yoon, Enhanced Durability and Catalytic Performance of Pt–SnO_2/Multi-Walled Carbon Nanotube with Shifted d-Band Center for Proton-Exchange Membrane Fuel Cells, Small Struct. 5 (2024) 2300407, https://doi.org/10.1002/sstr.202300407.

[23] A.R. Dhanya, D. Ganguly, R. Sundara, High temperature annealed (002) oriented WO_3 nanoplatelets with uniform Pt decoration as durable carbon free anode electrocatalyst for PEMFC application, Int. J. Hydrog. Energy 47 (2022) 24978–24990, https://doi.org/10.1016/j.ijhydene.2022.05.239.

[24] H. Huang, E.T.C. Hayes, D. Gianolio, G. Cibin, F.S. Hage, Q.M. Ramasse, A. E. Russell, Role of SnO_2 in the Bifunctional Mechanism of CO Oxidation at Pt-SnO_2 Electrocatalysts, ChemElectroChem 8 (2021) 2572–2582.

[25] D.V. Dao, G. Adilbish, T.D. Le, T.T.D. Nguyen, I.-H. Lee, Y.-T. Yu, Au@CeO_2 nanoparticles supported Pt/C electrocatalyst to improve the removal of CO in methanol oxidation reaction, J. Catal. 377 (2019) 589–599, https://doi.org/10.1016/j.jcat.2019.07.054.

[26] A. Aryafar, M.-S. Ekrami-Kakhki, A. Naeimi, Enhanced electrocatalytic activity of Pt-SnO_2 nanoparticles supported on natural bentonite-functionalized reduced graphene oxide-extracted chitosan from shrimp wastes for methanol electro-oxidation, Scientifc Reports 13 (2023) 3597, https://doi.org/10.1038/s41598-023-30705-w.

[27] S. Stevanović, D. Tripković, A. Gavrilović-Wohlmuther, J. Rogan, U. Lačnjevac, V. Jovanović, Carbon Supported PtSn versus $PtSnO_2$ Catalysts in Methanol Oxidation, Int. J. Electrochem. Sci. 16 (2021) 210222. https://doi.org/10.20964/2021.02.55.

[28] T. Takeguchi, A. Kunifuji, N. Narischat, M. Ito, H. Noguchi, K. Uosaki, S.R. Mukai, Ligand effect of SnO_2 on a PtRu catalyst and the relationship between bond strength and CO tolerance, Catal, Sci. Technol. 6 (2016) 3214–3219, https://doi.org/10.1039/c5cy01523e.

[29] M. Watanabe, S. Motoo, Electrocatalysis by ad-atoms: Part III, Enhancement of the Oxidation of Carbon Monoxide on Platinum by Ruthenium Ad-Atoms, Journal of Electroanalytical Chemistry and Interfacial Electrochemistry 60 (1975) 275–283, https://doi.org/10.1016/S0022-0728(75)80262-2.

[30] H. Zhu, X. Li, F. Han, Z. Dong, G. Yuan, G. Ma, A. Westwood, K. He, The effect of pitch-based carbon fiber microstructure and composition on the formation and growth of SiC whiskers via reaction of such fibers with silicon source, Carbon 99 (2016) 174–185, https://doi.org/10.1016/j.carbon.2015.12.002.

[31] S. Tahmasebi, S. Jahangiri, N. Mosey, G. Jerkiewicz, S. Baranton, C. Coutanceau, Y. Furuya, A. Ohma, Oxidation and Corrosion of Platinum−Nickel and Platinum−Cobalt Nanoparticles in an Aqueous Acidic Medium, ACS Appl. Energy Mater. 2 (2019) 7019–7035, https://doi.org/10.1021/acsaem.9b00625.

[32] S. Nagarani, G. Sasikala, K. Satheesh, M. Yuvaraj, R. Jayavel, Synthesis and characterization of binary transition metal oxide/reduced graphene oxide nanocomposites and its enhancedelectrochemical properties for supercapacitor applications, J. Mater. Sci. Mater. Electron. 29 (2018) 11738–11748, https://doi.org/10.1007/s10854-018-9272-0.

[33] A. Debataraja, D.W. Zulhendri, B. Yuliarto, H. Nugraha, B. Sunendar, Investigation of Nanostructured SnO_2 Synthesized with Polyol Technique for CO Gas Sensor applications, Procedia Engineering 170 (2017) 60–64, https://doi.org/10.1016/j.proeng.2017.03.011.

[34] X. Wang, L. Altmann, J. Stöver, V. Zielasek, M. Baumer, K. Al-Shamery, H. Borchert, J. Parisi, J. Kolny-Olesiak, Pt/Sn Intermetallic, Core/Shell and Alloy Nanoparticles: Colloidal Synthesis and Structural Control, Chem. Mater. 25 (2013) 1400–1407, https://doi.org/10.1021/cm302077w.

[35] J.F. Moulder, W.F. Stickle, P.E. Sobol, K.D. Bomben, Handbook of X-ray Photoelectron Spectroscopy: a Reference Book of Standard Spectra for Identification and Interpretation of XPS Data, in: J. Chastain (Ed.), Physical Electronics Division, Perkin-Elmer Corp, Eden Prairie, MN, 1992.

[36] G. Wang, T. Takeguchi, T. Yamanake, E.N. Muhamad, M. Mastuda, W. Ueda, Effect of preparation atmosphere of Pt-SnO_x/C catalysts on the catalytic activity for H_2/CO electro-oxidation, Appl. Catal B. : Environ. 98 (2010) 86–93, https://doi.org/10.1016/j.apcatb.2010.05.016.

[37] D.R.M. Godoi, J. Perez, H.M. Villullas, Alloys and oxides on carbon-supported Pt–Sn electrocatalysts for ethanol oxidation, J. Power Sources 195 (2010) 3394–3401, https://doi.org/10.1016/j.jpowsour.2009.12.037.

[38] X. Wang, J. Stöver, V. Zielasek, L. Altmann, K. Thiel, K. Al-Shamery, M. Bäumer, H. Borchert, J. Parisi, J. Kolny-Olesiak, Colloidal Synthesis and Structural Control of PtSn Bimetallic Nanoparticles, Langmuir 27 (2011) 11052–11061, https://doi.org/10.1021/la201829y.

[39] C.J. Powell, Elemental binding energies for X-ray photoelectron spectroscopy, Appl. Surf. Sci. 89 (1995) 141–149, https://doi.org/10.1016/0169-4332(95)00027-5.

[40] M. Galeotti, A. Atrei, U. Bardi, G. Rovida, M. Torrini, Surface alloying at the Sn-Pt (111) interface: a study by X-ray photoelectron diffraction, Surf. Sci. 313 (1994) 349–354, https://doi.org/10.1016/0039-6028(94)90055-8.

[41] A. Virnovskaia, S. Jørgensen, J. Hafizovic, Ø. Prytz, E. Kleimenov, M. Hävecker, H. Bluhm, A. Knop-Gericke, R. Schlögl, U. Olsbye, *In situ* XPS investigation of Pt (Sn)/Mg(Al)O catalysts during ethane dehydrogenation experiments, Surf. Sci. 601 (2007) 30–43, https://doi.org/10.1016/j.susc.2006.09.002.

[42] L.-P. Yuan, W.-J. Jiang, X.-L. Liu, Y.-H. He, C. He, T. Tang, J. Zhang, J.-S. Hu, Molecularly Engineered strong Metal Oxide−Support Interaction Enables Highly Efficient and Stable CO_2 Electroreduction, ACS Catal. 10 (2020) 13227–13235, https://doi.org/10.1021/acscatal.0c03831.

[43] K. Sang, J. Zuo, X. Zhang, Q. Wang, W. Chen, G. Qian, X. Duan, Towards a molecular understanding of the electronic metal-support interaction (EMSI) in heterogeneous catalysis, Green, Energy Environ. 8 (2023) 619–625, https://doi.org/10.1016/j.gee.2022.12.006.

[44] J. Ma, C. Canaff, N. Alonso-Vante, The effect of tuning and origin of tolerance to organics of platinum catalytic centers modified by selenium, Phys. Status Solidi A 211 (2014) 2030–2034, https://doi.org/10.1002/pssa.201330148.

[45] P.K. Babu, A. Lewera, J.H. Chung, R. Hunger, W. Jaegermann, N. Alonso-Vante, A. Wieckowski, E. Oldfield, J. Am. Chem. Soc. 129 (2007) 15140–15141, https://doi.org/10.1021/ja077498qCCC.

[46] W. Cao, Y. Mao, B. Hu, Y. Yang, W. Zhou, Z. Shao, Significantly improved stability and water retention for Pt supported on W-doped SnO_2 to catalyse the oxygen reduction reaction in proton exchange membrane fuel cells, J. Mater. Chem. A 12 (2024) 10799–10807, https://doi.org/10.1039/d4ta00388h.

[47] A.S. Abou- Elyazed, S. Hassan, A.G. Ashry, M. Hegazy, Facile,, Efficient, and cheap Electrode based on SnO_2/Activated Carbon Waste for Supercapacitor and Capacitive Deionization applications, ACS Omega 7 (2022) 19714–19720, https://doi.org/10.1021/acsomega.2c01458.

[48] S. Rudi, C. Cui, L. Gan, P. Strasser, Comparative Study of the Electrocatalytically active Surface areas (ECSAs) of Pt Alloy Nanoparticles Evaluated by H_{upd} and CO-stripping voltammetry, Electrocatalysis 5 (2014) 408–418, https://doi.org/10.1007/s12678-014-0205-2.

[49] E. Lebègue, S. Baranton, C. Coutanceau, Polyol synthesis of nanosized Pt/C electrocatalysts assisted by pulse microwave activation, J. Power Sources 196 (2011) 920–927, https://doi.org/10.1016/j.jpowsour.2010.08.107.

[50] S. Harish, S. Baranton, C. Coutanceau, J. Joseph, Microwave assisted polyol method for the preparation of Pt/C, Ru/C and PtRu/C nanoparticles and its application in electrooxidation of methanol, J. Power Sources 214 (2012) 33–39, https://doi.org/10.1016/j.jpowsour.2012.04.045.

[51] F.K. Bouho, T. Rafaïdeen, T.W. Napporn, C. Coutanceau, Behaviour of $Pt_{10-x}Ru_x/C$ catalysts towards the hydrogen oxidation reaction in acidic medium in the presence of adsorbed CO, Electrochim. Acta 498 (2024) 144697, https://doi.org/10.1016/j.electacta.2024.144697.

[52] H. Huang, O.F. Blackman, V. Celorrio, A.E. Russell, Isolating the contributions of surface Sn atoms in the bifunctional behaviour of PtSn CO oxidation electrocatalysts, Electrochim. Acta 390 (2021) 138811, https://doi.org/10.1016/j.electacta.2021.138811.

[53] V. Stamenković, M. Arenz, B.B. Blizanac, K.J. Mayrhofer, P.N. Ross, N. M. Marković, In situ CO oxidation on well characterized Pt_3Sn(hkl) surfaces: a selective review, Surf. Science 576 (2005) 145–157, https://doi.org/10.1016/j.susc.2004.12.018.

[54] M. Arenz, V. Stamenković, B.B. Blizanac, K.J. Mayrhofer, N.M. Marković, P. N. Ross, Carbon-supported Pt–Sn electrocatalysts for the anodic oxidation of H_2, CO, and H_2/CO mixtures: Part II: the structure–activity relationship, J. Catal. 232 (2005) 402–410, https://doi.org/10.1016/j.jcat.2005.03.022.

[55] D. Shen, F. Sun, Z. Liang, B. Mei, Y. Xie, Y. Wang, L. Wang, H. Fu, Oxygen spillover on supported Pt-cluster for anti-CO-poisoning hydrogen oxidation, Nat. Comm. 16 (2025) 3883, https://doi.org/10.1038/s41467-025-58735-0.

[56] G.N. Vayssilov, Y. Lykhach, A. Migani, T. Staudt, G.P. Petrova, N. Tsud, T. Skála, A. Bruix, F. Illas, K.C. Prince, V. Matolín, K.M. Neyman, J. Libuda, Support nanostructure boosts oxygen transfer to catalytically active platinum nanoparticles, Nat. Mater. 10 (2011) 310–315, https://doi.org/10.1038/nmat2976.

[57] H. Cheng, W. Lin, X. Li, C. Zhang, F. Zhao, Selective Hydrogenation of m-Dinitrobenzene to m-Nitroaniline over Ru-SnO_x/Al_2O_3 Catalyst, Catalysts 4 (2014) 276–288, https://doi.org/10.3390/catal4030276.

[58] H. Chen, M. Yang, J. Liu, G. Lu, X. Feng, Insight into the effects of electronegativity on the H_2 catalytic activation for CO_2 hydrogenation: four transition metal cases from a DFT study, Catal, Sci. Technol. 10 (2020) 5641–5647, https://doi.org/10.1039/d0cy01009j.

[59] N.M. Markovic, B.N. Grgur, P.N. Ross, Temperature-Dependent Hydrogen Electrochemistry on platinum Low-Index Single-Crystal Surfaces in Acid Solutions, J. Phys. Chem. B 101 (1997) 5405–5413, https://doi.org/10.1021/jp970930d.

[60] T. Shinagawa, A.T. Garcia-Esparza, K. Takanabe, Insight on Tafel slopes from a microkinetic analysis of aqueous electrocatalysis for energy conversion, Sci. Rep. 5 (2015) 13801, https://doi.org/10.1038/srep13801.

[61] J. Liu, B. Zhang, Y. Fo, J. Gao, W. Yu, H. Ren, X. Cui, X. Zhou, L. Jiang, Unique Ru nanoclusters confined in carbon molecular sieve coatings with tailoring sub-4 Å ultramicropores as a highly efficient and CO-tolerant hydrogen oxidation electrocatalyst, Chem. Eng. J. 468 (2023) 143438.

[62] Temperature (2025) accessed June 26, https://www.engineeringtoolbox.com/gases-solubility-water-d_1148.html.